nanomaterials

MDPI

Article

Aqueous Phase Synthesis of CuIn Alloy Nanoparticles and Their Application for a CIS ($CuInSe_2$)-Based Printable Solar Battery

Hideyuki Takahashi [1,*], Hironari Fujiki [1], Shun Yokoyama [1], Takayuki Kai [2] and Kazuyuki Tohji [1]

[1] Graduate school of Environmental studies, Environmentally Benign Systems, Tohoku University, Sendai 980-8579, Japan; hideyuki@mail.kankyo.tohoku.ac.jp (H.F.); shun.yokoyama.c2@tohoku.ac.jp (S.Y.); kazuyuki.tohji.a8@tohoku.ac.jp (K.T.)

[2] Panasonic Corp. Manufacturing Technology and Engineering Div., Osaka 571-8502, Japan; kai.takayuki@jp.panasonic.com

* Correspondence: hideyuki.takahashi.c2@tohoku.ac.jp; Tel.: +81-22-795-4854

Received: 14 March 2018; Accepted: 6 April 2018; Published: 6 April 2018



Abstract: To apply $CuInSe_2$ (CIS)-based printable solar batteries; an aqueous phase synthesis method of Cu-In (CI) alloy nanoparticles is studied. Metal complexes in the original solution are restricted to homogenized species by utilizing calculations. For example; $[(Cu^{2+})(ASP^{2-})_2]$ [ASP: the "body ($C_4H_5O_4N$)" of aspartic acid ($C_4H_7O_4N$)] is predominant in the pH 6–13 region ($C_{ASP}/C_{Cu} > 6$); while In complexes can be restricted to $[(In^{3+})(OH^-)(EDTA^{4-})]$ (pH 10–12; $C_{EDTA}/C_{In} = 2$) and/or $[(In^{3+})(ASP^{2-})_2]$ (pH 7–9; $C_{ASP}/C_{In} = 5$). These results indicate that the added amount of complex reagents should be determined by calculations and not the stoichiometric ratio. The reduction potential of homogenized metal complex is measured by cyclic voltammetry (CV) measurements and evaluated by Nernst's equation using the overall stability constants. CuIn alloy nanoparticles with a small amount of byproduct (In nanoparticles) are successfully synthesized. The CI precursor films are spin-coated onto the substrate using a 2-propanol dispersion. Then the films are converted into CIS solar cells; which show a maximum conversion efficiency of 2.30%. The relationship between the open circuit potential; short circuit current density; and fill factor indicate that smoothing of the CIS films and improving the crystallinity and thickness increase the solar cell conversion efficiency.

Keywords: metal complex; control; aqueous phase synthesis

1. Introduction

Actualization of environmental problems has increased research that utilizes natural energy [1–3]. Recently, Si-based solar batteries have been widely used in effective natural energy conversion devices. However, the minimum energy payback time is ca. 1.5 years because the reduction of SiO_2 to Si has an extremely large energy consumption (−856.7 J/mol) [4,5]. However, increasing the conversion efficiency will decrease the energy payback time, but drastically changing a Si-based solar battery's efficiency is challenging as its actual efficiency has already reached 25% and the theoretical value is ca. 28% [6,7]. Therefore, various types of solar batteries have been vigorously researched.

Thin film-based solar batteries [8] have been intensively studied due to their attractive characteristics, such as a relatively high efficiency [7], resource conservation [9,10], simple synthesis, etc. [11,12]. Since $CuInSe_2$ (CIS)-based solar batteries are attractive solar cell materials [13] with a maximum efficiency up to 20.9% and long lifetimes in large scale modules, commercialization of CIS-based solar batteries is stimulated [14].

A CIS-based solar battery is mainly synthesized utilizing the gas phase deposition method [15,16]. This synthesis consumes a large amount of natural resources and has a high energy loss because the vapors of individual elements are widely spread and accumulate on the substrate in various concentrations [16–18]. Furthermore, the solar cell's shape and size are limited by the reaction apparatus' dimensions. Thus, many studies have tried to synthesize CIS materials by the chemical reduction method, which is an ecological and economical technique. For example, Ye et al., synthesized Cu-In alloy particles via chemical reduction in an organic solvent in which the Cu-In alloy precursor films were transformed into $CuInSe_2$ films by a selenide procedure [19]. The resulting cells demonstrated a maximum energy conversion efficiency of 3.92% [19]. However, the total cost of this method is not low since this procedure requires an organic solvent, such as tetraethylene glycol ($C_8H_{18}O_5$, TEG). Therefore, Shih-Hsien et al. synthesized Cu-In alloy nanoparticles in an aqueous phase using metal salts and triethylamine as a stabilizing reagent; selenide materials showed an energy conversion efficiency of 1.47% [20]. Unfortunately, the synthetic mechanism in the aqueous solution remains unclear, and their process cannot be widely applied to prepare other compositions or materials.

Although metallic nanoparticles are easily synthesized in the liquid phase by the reduction of metal ions and/or complexes, core-shell materials and/or amorphous-like materials are sometimes formed. The former appears when the reduction rate of each metal ion and/or complex differs, while the latter is synthesized when a strong reducing agent is used. Therefore, to synthesize uniform and well-crystallized alloy nanoparticles, Takahashi et al. controlled the homogenization of the metallic complexes in an aqueous solution at room temperature by using calculations, EXAFS (extended X-ray absorption fine structure), and ESI-TOF-MS (electrospray ionization time of flight mass spectroscopy) analyses [21,22]. Consequently, uniform and well-crystallized alloy nanoparticles, such as $Pd_{20}Te_7$ and Bi_2Te_3, were successfully synthesized [22,23].

Co-deposition of Cu and In ions is relatively difficult since the reduction potentials of these ions differ greatly (0.342 V for Cu and −0.338 V for In) [24,25]. However, the reduction potential of the metal complex is not the same as that of the ion. This means that the difference in the reduction potential of each metal can be freely controlled using metal complex species (i.e., critical stability constants) and that of the ratio in aqueous solution should realize uniform and well-crystallized CuIn alloy nanoparticles.

In this study, the synthesis and its mechanism to form Cu-In alloy nanoparticles are elucidated. Moreover, the synthesized materials are applied to form CIS-based printable solar batteries.

2. Experimental

2.1. Calculations

Copper nitrate (Wako Chemicals, Japan, $Cu(NO_3)_2 \bullet 3H_2O$) and indium nitrate (Wako Chemicals, $InNO_3 \bullet 3H_2O$) were used as the Cu and In precursor salts, respectively. Citric acid (Wako Chemicals, $C_6H_8O_7$), maleic acid (Wako Chemicals, $C_4H_4O_4$), glycine (Wako Chemicals, $C_2H_5O_2N$), ethylenediamine (Wako Chemicals, $C_2H_8N_2$, called as "EDA"), nitrilotriacetic acid (Wako Chemicals, $C_6H_9O_6N$), ethylenediaminetetraacetic acid (Wako Chemicals, $C_{10}H_{16}O_8N_2$, "EDTA"), oxalic acid (Wako Chemicals, $C_2H_2O_4$), and aspartic acid (Wako Chemicals, $C_4H_7O_4N$) were used as complex reagents. The concentrations of Cu and/or In complexes at various pH values of the aqueous solution were calculated using the critical stability constants. The calculation method is described in the literature [21].

For example, briefly, calculation methods for Cu ion-aspartic acid-OH^--NO_3^- system were performed as follows: Aspartic acid ($C_4H_7O_4N$, H_2L) is denoted as H_2 ($C_4H_5O_4N$). Thus, the "L" of aspartic acid is $C_4H_5O_4N$, which is denoted as ASP. As such, various complex species in the solution are described as follows, where Kx are the critical stability constants:

$[H(ASP)] = K1[H][ASP]$	LogK1 = 9.65
$[(H)_2(ASP)] = K2[H(ASP)][H]$	LogK2 = 3.70
$[(H)_3(ASP)] = K3[(H)_2ASP][H]$	LogK3 = 1.90
$[Cu(ASP)] = K4[Cu][\ ASP]$	LogK4 = 8.88
$[Cu(ASP)_2] = K5[Cu][\ ASP]^2$	LogK5 = 15.6
$[Cu(H)(ASP)] = K6[Cu(ASP)][H]$	LogK6 = 3.70
$[Cu(H)(ASP)_2] = K7[Cu(ASP)_2][H]$	LogK7 = 4.00
$[(Cu)_2(ASP)] = K8[Cu(ASP)][Cu]$	LogK8 = 1.51
$[(Cu)_2(ASP)_2] = K9[Cu(ASP)_2]\ [Cu]$	LogK9 = 3.60
$[Cu(OH)] = K10[Cu][OH]$	LogK10 = 6.50
$[Cu(OH)_2] = K11[Cu][OH]^2$	LogK11 = 11.8
$[Cu(OH)_3] = K12[Cu][OH]^3$	LogK12 = 14.5
$[Cu(OH)_4] = K13[Cu][OH]^4$	LogK13 = 16.4
$[(Cu)_2(OH)] = K14[Cu]^2[OH]$	LogK14 = 8.20
$[(Cu)_2(OH)_2] = K15[Cu]^2[OH]^2$	LogK15 = 17.7
$[(Cu)_3(OH)_4] = K16[Cu]^3[OH]^4$	LogK16 = 35.2
$[Cu(NO_3)] = K17[Cu][NO_3]$	LogK17 = −0.13
$[Cu(NO_3)_2] = K18[Cu][NO_3]^2$	LogK18 = −0.60

Here, C_{Cu} is the sum of the Cu complexes and ions. Therefore:

$$C_{Cu} = [Cu] + K4[Cu][ASP] + K5[Cu][\ ASP]^2 + K6[Cu(ASP)][H] + K7[Cu(ASP)_2][H] + 2K8[Cu(ASP)][Cu] + 2\ K9[Cu(ASP)_2]\ [Cu] + K10[Cu][OH] + K11[Cu][OH]^2 + K12[Cu][OH]^3 + K13[Cu][OH]^4 + 2K14[Cu]^2[OH] + 2K15[Cu]^2[OH]^2 + 3K16[Cu]^3[OH]^4 + K17[Cu][NO_3] + K18[Cu][NO_3]^2$$

In the same manner, C_{ASP} (total amount of ASP species) and $C_{NO_3^-}$ (total amount of NO_3^- species) can describes as follows:

$$C_{ASP} = [ASP] + K1[H][ASP] + K2[H(ASP)][H] + K3[(H)_2(ASP)][H] + K4[Cu][ASP] + 2K5[Cu][\ ASP]^2 + K6[Cu(ASP)][H] + 2K7[Cu(ASP)_2][H] + K8[Cu(ASP)][Cu] + 2\ K9[Cu(ASP)_2]\ [Cu]$$

$$C_{NO_3^-} = [NO_3] + K17[Cu][NO_3] + K18[Cu][NO_3]^2$$

From the simultaneous equations of C_{Cu} and C_{ASP} and C_{NO_3}, the ratio of each complex can be calculated.

2.2. Reduction Potential Measurements of Homogenized Cu Complexes

The reduction potentials of homogenized Cu complexes were measured via the cyclic voltammetry method (GAMRY, Reference 600, Potentiostat/Galvanostat/ZRA, called as CV). Platinum wire, Au plate, and Ag/AgCl electrodes were used as the counter electrode, working electrode, and reference electrode, respectively.

2.3. Preparation and Selenization Method of Cu-In Alloy Nanoparticles

Cu-In alloy nanoparticles were prepared as follows. Aqueous solutions of 8–10 mmol/L $Cu(Cl)_2 \bullet 2H_2O$ (Wako Chemical, >99%), 10 mmol/L $In(Cl)_3 \bullet 4H_2O$ (Wako Chemical, >97%), 0.5 mol/L aspartic acid (Wako Chemical, >97%), were introduced into a glass vessel and mixed well. As necessary, polyvinylpyrrolidone (Wako Chemical, PVP (K25) and/or PVP(K16–18)) was added. The pH was adjusted to 9 with a NaOH aqueous solution, and the final volume was adjusted to 40 mL. Then 10 mmol of a $NaBH_4$ solution (10 mL, 30 °C) whose pH was similar to the metal complex solution was introduced into the glass vessel, and mixed at 30 °C for 1 h. The synthesized materials were collected, washed with EtOH, and dried.

The synthesized Cu-In nanoparticles (1.5 g) were well dispersed into 7.5-mL 2-PrOH by ultrasonic wave irradiation for 60 min. The synthesized Cu-In alloy nanoparticle dispersion was spin-coated onto a Mo/glass substrate and dried at 200 °C. Selenization of the Cu-In nanoparticle film on a Mo/glass substrate was performed under a 9.6×10^{-2} Pa H_2Se gas atmosphere (total pressure: 0.6 atm). The treatment temperature was changed from 300 °C to 575 °C at a constant treatment time of 1 h.

2.4. Evaluation of the Synthesized Materials

The synthesized materials were evaluated by XRD (Rigaku Co., Ltd., Japan. MULTI FLEX, 40 kV, 20 mA), SEM (Hitachi Co., Ltd., Japan. SU8000), Raman spectroscopy (HORIBA JOBIN YVON, T64000). I-V measurements and quantum effectivity measurements were performed using cells formed by a CIS film (*p*-type semiconductor) and a CdS film (*n*-type semiconductor).

3. Results and Discussion

Figure 1 shows the calculation results for the Cu-aspartic acid-OH system (C_{Cu} = 0.01 mol/L, C_{NO_3} = 0.02 mol/L and $C_{aspartic\ acid}$ = 0.06 mol/L), which reveal the relationship between the ratio of Cu complexes (vertical axis) and pH (horizontal axis). As already mentioned, aspartic acid ($C_4H_7O_4N$, H_2L) is denoted as H_2 ($C_4H_5O_4N$). Thus, the "L" of aspartic acid is $C_4H_5O_4N$, which is denoted as ASP^{2-}. Various Cu-aspartic acid complexes such as $[(Cu^{2+})(H^{+})(ASP^{-})]$ and Cu ions form in acidic conditions, However, $[(Cu^{2+})(ASP^{2-})_2]$ is predominant in the pH region of 6–13. These results suggest that the Cu complex can be homogenized if the solution is adjusted to the above conditions. It should be noted that homogenization is successfully achieved in the case of $C_{ASP}/C_{Cu} > 6$ (=0.06/0.01), which is not obtained by the addition of stoichiometric amounts.

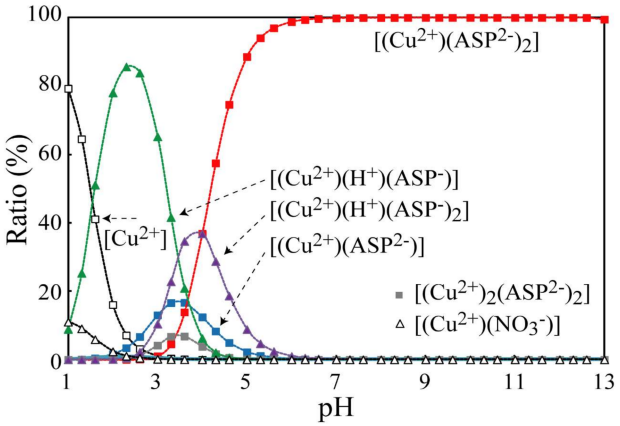


Figure 1. Results of the calculation in the cases of Cu-ASP-OH system as a function of pH, (C_{Cu} = 0.01 mol/L, C_{NO_3} = 0.02 mol/L, and C_{ASP} = 0.06 mol/L).

Table 1 summarizes the relationship between homogenized species and the solution condition calculated in the case of each complex reagent. The "L" of oxalic acid (H_2L), EDA (L), NTA (H_3L), EDTA(H_4L), maleic acid (H_2L), citric acid (H_3L), and glycine (HL) are denoted as "oxa", "EDA", "NTA", "EDTA", "mal", "cit", and "gly", respectively. The Cu complexes are restricted to $[(Cu^{2+})(oxa^{2-})_2]$ (pH 3–10), $[(Cu^{2+})(gly^{-})_2]$ (pH 6–12), $[(Cu^{2+})(EDA)_2]$ (pH 7–12) and $[(Cu^{2+})(NTA^{3-})_2]$ (pH 8–11). $[(Cu^{2+})(EDTA^{4-})]$ (pH 5–10), $[(Cu^{2+})_2(OH^{-})_2(mal^{2-})_2]$ (pH 9–12), and $[(Cu^{2+})_2(OH^{-})_2(cit^{3-})_2]$ (pH 7–12) are predominant in the respective pH region. Similar to the case of aspartic acid, homogenization of Cu complex requires the addition of 1.5 times (NTA), two times (EDTA and EDA), three times (glycine), six times (maleic acid and citric acid), and 10 times (oxalic acid) of the complex reagents relative to Cu. On the other hand, the calculations for the In-complex reagents system demonstrate that In complexes can be restricted to $[(In^{3+})(OH^{-})(EDTA^{4-})]$ (pH 10–12, C_{EDTA}/C_{In} = 2) and/or $[(In^{3+})(ASP^{2-})_2]$ (pH 7–9, C_{ASP}/C_{In} = 5), respectively.

Cyclic voltammetry measurements of these homogenized metal complexes show peaks at −0.87 (V (vs. Ag/AgCl)) (oxa), −0.94 (V (vs. Ag/AgCl)) (gly), −1.08 (V (vs. Ag/AgCl)) (EDA), −1.01 (V (vs. Ag/AgCl)) (ASP), −0.98 (V (vs. Ag/AgCl)) (NTA), −1.05 (V (vs. Ag/AgCl)) (EDTA), −1.00 (V (vs. Ag/AgCl)) (mal), and −1.03 (V (vs. Ag/AgCl)) (cit).

Table 1. Relationship between homogenized species and solution condition calculated, and reduction potential in the case of oxalic acid, glycine, ethylenediamine (EDA), nitrilotriacetic acid (NTA), etylenediaminetetraacetic acid (EDTA), malic acid, and citric acid.

Complex Reagent	Concentration of Cu (mol/L)	Concentration of Complex Reagent (mol/L)	Homogenized Species	Ratio of Homogenized Species (%)	Reduction Potential [V(vs. Ag/AgCl)]
oxalic acid	0.01	0.1	$[(Cu^{2+})(oxa^{2-})_2]$	100	−0.87
glycine	0.01	0.03	$[(Cu^{2+})(gly^{-})_2]$	100	−0.94
EDA	0.01	0.02	$[(Cu^{2+})(EDA)_2]$	100	−1.08
ASP	0.01	0.06	$[(Cu^{2+})(ASP^{2-})_2]$	100	−1.01
NTA	0.01	0.03	$[(Cu^{2+})(NTA^{3-})_2]$	100	−0.98
EDTA	0.01	0.02	$[(Cu^{2+})(EDTA^{4-})]$	96.2	−1.05
malic acid	0.01	0.03	$[(Cu^{2+})_2(OH^{-})_2(mal^{2-})_2]$	92.8	−1.00
citric acid	0.01	0.06	$[(Cu^{2+})_2(OH^{-})_2(cit^{3-})_2]$	93.8	−1.03

The XRD measurement results of the films electrodeposited at the corresponding voltage (1800 sec) show apparent peaks of metallic Cu (PDF#04-0836) along with peaks of the Au substrate (PDF#04-0784). Thus, these voltages indicate the reduction potential of homogenized metal complexes (Table 1).

Here, the reduction potential of Cu metal from its oxide is clearly defined by the pH (i.e., potential-pH diagram). For example, that of Cu is −0.2 (V vs. SHE) [26]. On the other hand, that of Cu metal reduced from its complex shows another potential, which depends on the ligand species since the disconnection between Cu and the ligand is indispensable to reduce the Cu complex species (Table 1). The reduction potential shown in Table 1 can be recognized as that of Cu metal from its homogenized Cu complex, and it depends on the critical stability constants between Cu ion and ligands.

Among the consecutive stability constants and overall stability constants, the latter is relevant to the reduction of the Cu complex since the complex needs a perfect disconnection of the bonding between metal and ligands. The overall stability constants (K) can be described as follows:

$$K = k_1 \cdot k_2 \cdots\cdots k_n = \frac{[ML_n]}{\left[M(H_2O)_n\right][L]^2} \quad (1)$$

Figure 2 shows the relationship between LogK/*n* and the reduction potential of the homogenized Cu complexes. "n" means the valence of the metal in the complex. For example, n = 2 for $[(Cu^{2+})(Ligand)]$ and n = 4 for $[(Cu^{2+})_2(Ligand)]$. This relationship has a linear tendency.

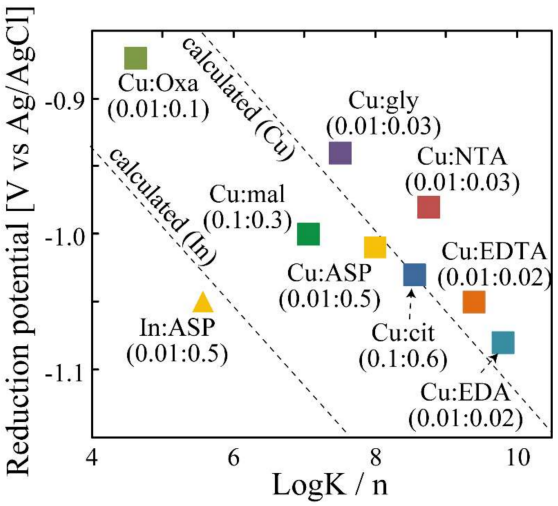


Figure 2. Relationship between LogK/n and reduction potential of homogenized Cu complexes. Reduction potential of Cu and In complexes calculated from Equations (8) and (9) were also inset in the figure (dotted line).

The reduction formula of [(M^{n+})(Ligand)] can be expressed as:

$$\left[\left(M^{n+}\right)L\right] + ne^{-} \rightarrow M + L \quad (2)$$

By utilizing Nernst's equation, the reduction potential of Equation (2) can be expressed as:

$$E = E_c^0 - \frac{RT}{nF} \cdot \ln \frac{L}{\left[\left(M^{n+}\right)L\right]} \quad (3)$$

On the other hand, when the metal ion (M^{n+}) and ligand (L) form a complex with the stability constants K, K is expressed as:

$$M^{n+} + L \rightarrow \left[\left(M^{n+}\right)L\right] \quad (4)$$

$$K = \frac{\left[\left(M^{n+}\right)L\right]}{\left[M^{n+}\right][L]} \quad (5)$$

Thus, the standard electrode potential of metal complex can be summarized as:

$$E = E_c^0 + \frac{RT}{nF} \cdot \ln K + \frac{RT}{nF} \rightarrow \ln\left[M^{n+}\right] \quad (6)$$

$$E_c^0 = E_0 - \frac{RT}{nF} \cdot \ln K \quad (7)$$

Here, the temperature (T) is 298 (K), gas constant (R) is 8.31 (J K^{-1} mol^{-1}), the Faraday constant (F) is 96,500 (C mol^{-1}), and the reduction potential of "bare" Cu ion (E_0) is −0.525 (V vs. Ag/AgCl) [27]. Therefore, the reduction potential of Cu metal complex can be expressed as:

$$E_c^0 = -0.525 - 0.059 \cdot \frac{\log K}{n} \quad (8)$$

In the same manner, considering the reduction potential of "bare" In ion (E_0 = −0.700 (V vs. Ag/AgCl) [28]), the reduction potential of the In metal complex can be expressed as:

$$E_c^0 = -0.700 - 0.059 \cdot \frac{\log K}{n} \quad (9)$$

The relationship between the reduction potential and the stability constants of Cu and In complexes calculated from Equations (8) and (9) (dotted line in Figure 2) are consistent with the measured values. Therefore, the reduction potential of the homogenized metal complex can be determined from these equations and the overall stability constants. In this study, alloy nanoparticles are synthesized using reducing agents with a specific potential. Thus, the low potential deference of both metal complexes, Δ(Cu-In), is significant in the synthesis of alloy nanoparticles. Taking these facts into consideration, it is expected that aspartic acid is a suitable ligand for Cu and In since Δ(Cu-In) is low (0.04). Actually, the XRD peaks (Figure 3) according with CuIn alloy (PDF#35-1150), Cu_2In alloy (PDF#42-1475), and In (PDF#05-0642) are detected from the film electrodeposited by using 0.01 M $Cu(NO_3)_2$-0.01 M $In(NO_3)_3$-0.50 M aspartic acid aqueous solution (pH 9) at −1.06 V (V (vs. Ag/AgCl)). These results indicate that Cu-In alloy nanoparticles can be synthesized under this condition.

Thus, chemical reduction was performed by using 0.01 M $Cu(NO_3)_2$-0.01 M $In(NO_3)_3$-0.50 M aspartic acid aqueous solution (pH 9) and 0.1 M $NaBH_4$ solution as a reducing reagent. Due to the coordination of water molecules to In in the presence of NO_3^- ion [27], the synthesized precipitate was re-dissolved into solution during filtration and the drying process. Therefore, metal salts were

changed from nitrates to chlorides. Cu-chloride or In-chloride complexes are not formed in this solution condition.

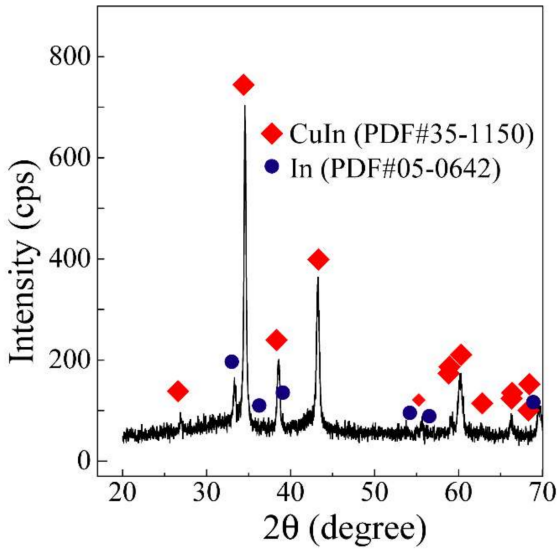


Figure 3. XRD profile of the material synthesized from the 0.01 M $CuCl_2$-0.01 M $InCl_3$-0.50 M ASP aqueous solution (pH 9, 30 °C, reaction time was 1 h).

From the XRD profile of the material synthesized from the 0.01 M $CuCl_2$-0.01 M $InCl_3$-0.50 M aspartic acid aqueous solution (pH 9, 30 °C, reaction time of 1 h) and 0.1 M $NaBH_4$ solution, many peaks corresponding to CuIn (PDF#35-1150) and small peaks of In (PDF#05-0642) are clearly observed. The recovery rate is >98%. It is well known that In can co-exist in the η phase (Cu_2In) below 157 °C, as shown in the Cu-In binary phase diagram [28,29]. It is also true that the CuIn alloy phase is also obtained frequently in thermodynamically slow syntheses, leading to a nonequivalent state. This experiment used thermodynamically slow conditions (e.g., 30 °C) [30–34]. For example, a mixture of CuIn/In/Cu_2In has been synthesized in other reports [21,35].

From the above results, it is clear that Cu-In alloy nanoparticles can be synthesized in the aqueous phase at room temperature. However, their particle size varies widely (20–600 nm), which is not suitable for CIS-based printable solar batteries. Therefore, we tried to control the particle diameter (PD) and standard deviation (SD) of the synthesized alloy nanoparticles.

Figure 4 shows the SEM micrographs of Cu-In alloy nanoparticles synthesized with (a) 2.5 mM CTAB, (b) 2.5 mM SDS, (c) 2.5 mg/50mL PVP(K25), and (d) 2.5 mg/50 mL PVP(K16–18), respectively. The PD/SD calculated from 200 particles drastically changes (i.e., 88 nm/41 (CTAB 2.5 mM), 76 nm/31 (SDS, 2.5 mM), 31 nm/12 (PVP(K16–18), 2.5 mg/50 mL), 47 nm/19 (PVP(K25), and 2.5 mg/50 mL)). Here, the basic structures of PVP(K16–18) and PVP(K25) are almost the same, but the polymerization degree of the vinyl groups differ. The length of the former is ca. 79 nm, while that of latter is ca. 350 nm. On the other hand, the synthesized particle size is ca. 50 nm.

Taking the previously report, which mentioned the relationship between the length of the vinyl groups in PVP and the secondary particle size, into consideration [36], the particle size control mechanism is as follows: In the case of PVP(K16–18), Cu-In nanoparticles do not aggregate since the diameter and the length of PVP are almost the same. On the other hand, many Cu-In nanoparticles form secondary particles when PVP(K25) is used as the size-control reagent due to the intertwining of long functional groups around the particles.

Cu-In precursor films with relatively flat surfaces are successfully spin-coated onto the substrate via a 2-propanol dispersion of Cu-In alloy nanoparticles synthesized with PVP(K16–18). Figure 5 shows the XRD profiles of the Cu-In precursor films after selenization at 300, 400, 500, and 575 °C. The peaks of the CuIn alloy phase (PDF#35-1150) disappear, while those the $CuInSe_2$ phase (PDF#40-1487) and

the Cu_3Se_2 phase (PDF#47-1745) appear when Cu-In precursor films are selenized at 300 °C. As the treatment temperature increases to 400 °C, only the peaks of the $CuInSe_2$ phase (PDF#40-1487) are detected. However, at a treatment temperature of 575 °C, the peaks of the (103) and (211) planes of the $CuInSe_2$ phase, which indicate the existence of the chalcopyrite structure [37], are detected. Since the chalcopyrite structure of $CuInSe_2$ phase is essential to construct effective solar cells [38], the selenide temperature used in this experiment was 575 °C. Here, the Cu_2Se phase is sometimes co-synthesized with the $CuInSe_2$ phase as a byproduct [39]. However, we cannot identify the $CuInSe_2$ and Cu_2Se from the XRD profile because both have the same primitive lattice and almost the same lattice constants [40–43].

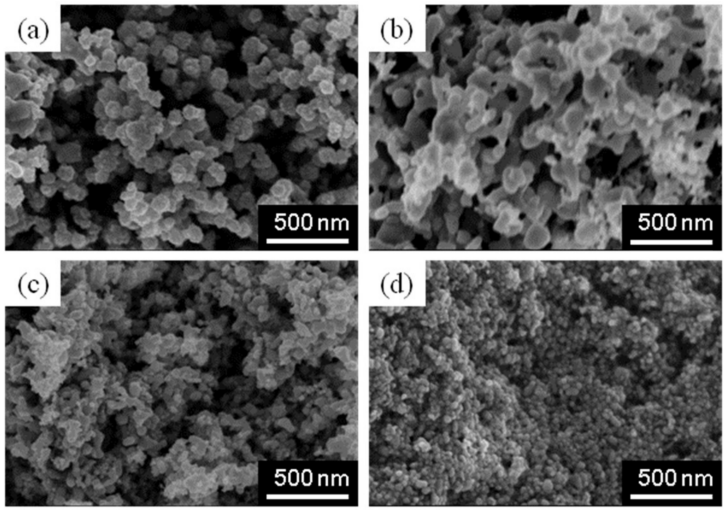


Figure 4. SEM micrographs of Cu-In alloy nanoparticles synthesized with (**a**) 2.5 mM CTAB; (**b**) 2.5 mM SDS; (**c**) 2.5 mg/50 mL PVP(K25); and (**d**) 2.5 mg /50 mL PVP(K16–18), respectively.

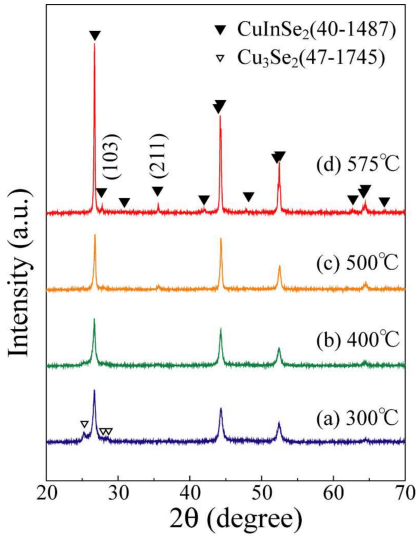


Figure 5. XRD profiles of Cu-In precursor films selenized at 300, 400, 500, and 575 °C.

The existence of Cu_2Se was evaluated by the Raman scattering measurement method. Figure 6 shows CIS films selenized at 300, 400, 500, and 575 °C. The peaks of $CuInSe_2$ are detected at 174 cm^{-1} (A_1 vibrational mode), 206 cm^{-1} (E mode), 215 cm^{-1} (B_2,E mode) and 231 cm^{-1} (B_2,E mode) [44], while a weak peak of Cu_2Se is also detected at 262 cm^{-1} [45]. Thus, the main phase of the CIS films synthesized in this study is $CuInSe_2$. Nevertheless, a very small amount of Cu_2Se phase is involved.

Taking the pseudo-binary phase diagram of Cu_2Se-In_2Se_3 into consideration [46], it expected that Cu_2Se will separate under the conditions of In_2Se_3 < 50 mo1% and T < 500 °C since $CuInSe_2$ (α phase) does not have a solid solution region. To restrict the synthesis of byproducts, the ratio of Cu against In should be less than 1.

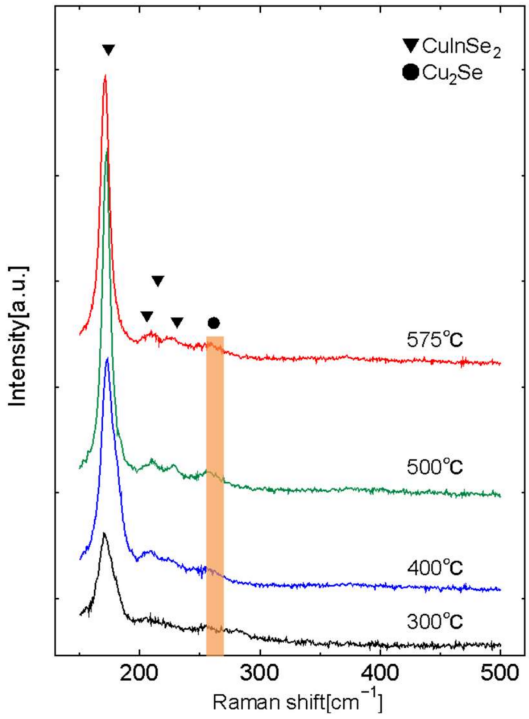


Figure 6. Results of Raman scattering measurements of the CIS films selenized at 300, 400, 500, and 575 °C.

Figure 7 shows the J-V measurement results of the CIS films, which were prepared using Cu-In nanoparticles synthesized at (a) PVP(K16–18) and Cu/In = 0.91; (b) PVP(K25) and Cu/In = 0.91; and (c) PVP(K25) and Cu/In = 0.81. The measurements were performed under irradiation of AM 1.5-G illumination and under dark conditions. Table 2 summarizes the open circuit potential (V_{OC} [mV]), short circuit current density (J_{SC} [mA/cm^2]), fill factor (FF), and conversion efficiency (η[%]) of each CIS solar cell.

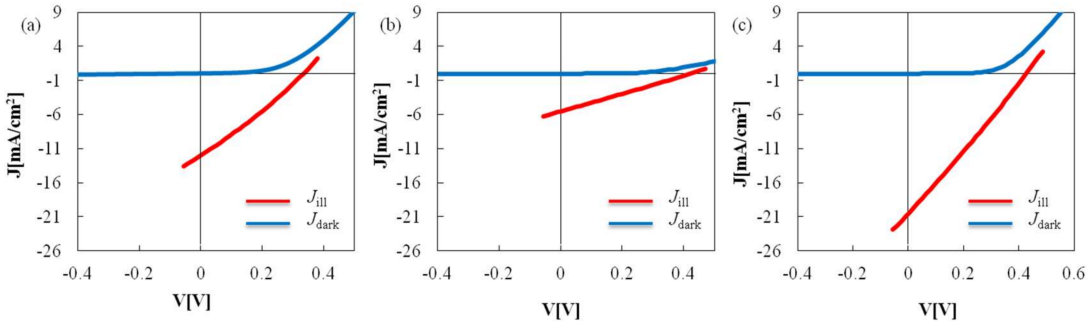


Figure 7. J-V measurement results of CIS films which constituted by using Cu-In nanoparticles synthesized at (**a**) PVP(K16–18) and Cu/In = 0.91; (**b**) PVP(K25) and Cu/In = 0.91; and (**c**) PVP(K25) and Cu/In = 0.81, under AM 1.5G illumination and in the dark.

Table 2. PV parameters evaluated from the J-V curves for the CIS solar cells.

Sample	V_{OC} (mV)	J_{SC} (mA/cm^2)	FF	η (%)
PVP(K16–18), Cu/In = 0.91	330	12.0	0.28	1.12
PVP(K25) Cu/In = 0.91	420	5.53	0.26	0.60
PVP(K25) Cu/In = 0.81	430	20.5	0.26	2.30

The CIS films synthesized from Cu-In alloy nanoparticles formed in an aqueous solution at room temperature act as solar cells. The maximum conversion efficiency (η) is 2.30%. These results indicate that the aqueous phase synthesized Cu-In alloy nanoparticles can applied to CIS-based printable solar batteries, although the efficiency of the CIS solar cell synthesized in this experiment is lower than that of the CIS solar cell synthesized under the gas phase condition (for example, η = 20.9% [14]).

There are three reasons why the efficiency of the solar battery synthesized in this experiment is lower than that synthesized in the gas phase: (1) recombination loss, (2) parasitic loss; and (3) optical loss. These losses induce the loss of (1) Voc, (2) FF, Jsc, Voc, and (3) Jsc [17]. The series resistance (Rse), parallel conductance (Gsh), ideality factor (n), saturation current density (J_0) of the solar battery's equivalent circuit can be calculated as follows: The J-V properties of the solar battery's equivalent circuit under darkness condition is expressed as [47]:

$$J = J_0 \exp\left[\frac{q}{nkT}(V - RseJ)\right] + GshV \quad (10)$$

Here, J_0 is the saturation current density (mA/cm^2), q is the quantum of electricity (1.602×10^{-19} (C)), and n is ideality factor of the diode. k is Boltzmann's factor (1.380×10^{-23} (J/K)), and T is temperature (K). Rse is the series resistance (Ω cm^2) and Gsh is the parallel conductance (mS/cm^2). If Equation (10) is differentiated with respect to V, Equation (11) is obtained:

$$\frac{dJ}{dV} = J_0\left[\frac{q}{nkT}(V - RseJ)\right]\exp\left[\frac{q}{nkT}V\right] + Gsh \quad (11)$$

In the region V < 0, $J_0\left[\frac{q}{nkT}(V - RseJ)\right]\exp\left[\frac{q}{nkT}V\right]$ approaches to 0 from the plot of V against to dJ/dV. Thus, the value where dJ/dV becomes constant is equivalent to Gsh in the region V < 0.

On the other hand, if Equation (10) is differentiated with respect to J, it expressed as:

$$\frac{dV}{dJ} = Rse + \frac{nkT}{q}J^{-1} \quad (12)$$

Thus, the y-intercept and gradient of the plot of J^{-1} against to dV/dJ are equal to Rse and nkT/q, respectively. From these, the value of Gsh, Rse, and n become clear. Transformation of Equation (10) yields, Equation (13):

$$\ln(J - GshV) = \frac{q}{nkT}(V - RseJ) + \ln J_0 \quad (13)$$

Thus, the y-intercept of the plot of V − RseJ against to ln(J − GshV) is equal to $\ln J_0$. From the relationship of these equations, Rse, Gsh, n, and J_0 can be calculated.

Figure 8 shows the (a) dJ/dV vs. V curves to evaluate Gsh; (b) dV/dJ vs. 1/J plot to determine Rse and n; and (c) semi-logarithmic plot of (j-GshV/A) vs. V-RJ to determine J_0. Table 3 summarizes the Gsh, Rse, n, and J_0, of the CIS devices synthesized in this study, as well as those for the gas phase condition. n and J_0 of the CIS devices synthesized in this experiment are higher than those of the gas phase synthesized CIS devices. These results mean that the CIS devices synthesized in this experiment involve many recombination losses, which lowers the open circuit potential.

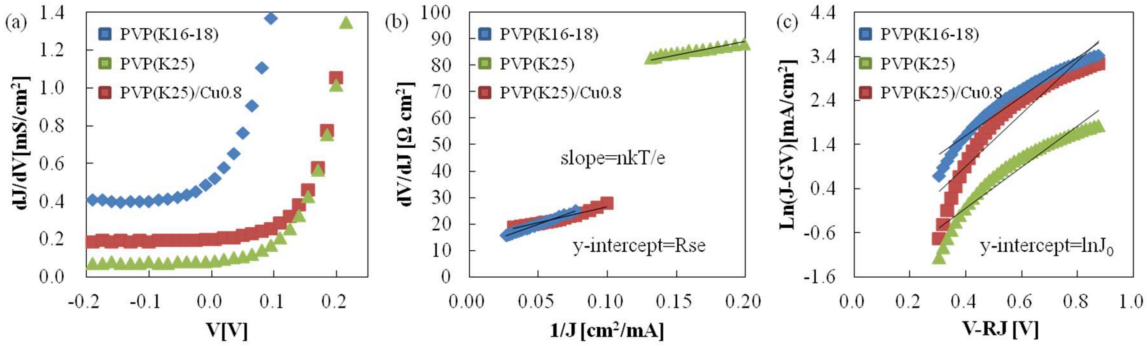


Figure 8. (**a**) dJ/dV vs. V curves for Gsh evaluation; (**b**) dV/dJ vs. 1/J plot for the determination of Rse and n; and (**c**) semilogarithmic plot of (j-GshV/A) vs. V-RJ for determination of J_0.

Table 3. Shunt conductance (Gsh), series resistance (Rse), ideality factor (n), and saturation current density (J_0) of CIS devices synthesized in this study and also gas phase condition.

Sample	Gsh (mS/cm^2)	Rse (Ω cm^2)	n	J_0 (mA/cm^2)
PVP(K16–18)	0.40	10.8	7.06	0.86
PVP(K25)	0.08	68.4	4.00	0.15
PVP(K25)/Cu0.8	0.20	14.3	4.71	0.23
CIGS(gas phase) (η = 15.5%)	0.05	0.20	1.50	2×10^{-6}

Figure 9 shows the SEM images (surface morphology and cross-section) of the CIS solar cells based on Cu-In nanoparticles using (a,d) PVP(K16–18) and Cu/In = 0.91, (b,e) PVP(K25) and Cu/In = 0.9, and (c,f) PVP(K25) and Cu/In = 0.81. In each case, it is apparent that the cell has a rough surface, which induces the lack of p-n junctions [19]. Moreover, crystal growth is limited to the surface area of the CIS films (<1 μm). The crystallinity inside the CIS films is low, and the thickness of the CIS solar cell is 4–6 μm, which is two or three times thicker than that of the effective CIS solar battery [48]. These characteristics increase the series resistance, leading to recombination loss that eventually results in the loss of FF, Jsc, and Voc. These results mean that the smoothing of the CIS films and improving the crystallinity and thickness induce the solar cells properties.

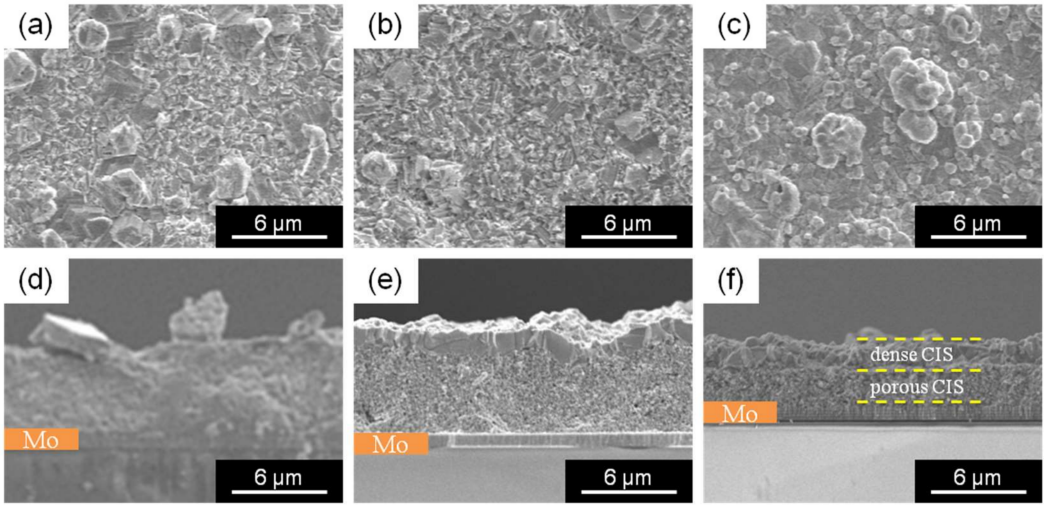


Figure 9. SEM images (surface morphology and cross-section) of the CIS solar cell based on Cu-In nanoparticles using (**a**,**d**) PVP(K16-18) and Cu/In = 0.91, (**b**,**e**) PVP(K25) and Cu/In = 0.9, (**c**,**f**) PVP(K25) and Cu/In = 0.81.

4. Conclusions

The calculations and CV measurements of homogenized complex species indicate that aspartic acid is a suitable ligand for Cu and In because Δ(Cu-In) is low (0.04). Under the appropriate conditions (0.01 M $CuCl_2$-0.01 M $InCl_3$-0.50 M aspartic acid aqueous solution (pH 9, 30 °C, reaction time was 1 h) and a 0.1 M $NaBH_4$ solution), CuIn alloy nanoparticles with In small peaks are successfully synthesized with a recovery rate of >98%. CIS films synthesized from Cu-In alloy nanoparticles act as solar cells with the maximum conversion efficiency of 2.30%. The results indicate that aqueous phase synthesized Cu-In alloy nanoparticles can be applied to CIS-based printable solar battery. This method should be applicable to various alloy synthesis systems.

Acknowledgments: This work was supported by JSPS KAKENHI grant number 26281054 and 17K18967.

Author Contributions: H.T. and K.T. conceived and designed the experiments; H.T. and H.F. and S.Y. and K.T. performed the experiments; H.T. and H.F. analyzed the data; H.T. and K.T. contributed reagents/materials/analysis tools; H.T. wrote the paper.

Conflicts of Interest: The authors declare no conflict of interest.

References

1. BP Group. *BP Statistical Review of World Energy June 2014*, 63rd ed.; BP Group: London, UK, 2014.
2. Intergovernmental Panel on Climate Change (IPCC). *Climate Change 2013: The Physical Science Basis*; IPCC: Geneva, Switzerland, 2013.
3. European Photovoltaic Industry Association (EPIA). *Global Market Outlook for Photovoltaics 2014–2018*; EPIA: Brussels, Belgium, 2014.
4. Wagman, D.D.; Evans, W.H.; Parker, V.B.; Schumm, R.H.; Halow, I. *The NBS Tables of Chemical Thermodynamic Properties. Selected Values for Inorganic and C_1 and C_2 Organic Substances in SI units*; American Chemical Society: Washington, DC, USA, 1982.
5. Espinosa, N.; García-Valverde, R.; Urbina, A.; Krebs, F.C. A life cycle analysis of polymer solar cell modules prepared using roll-to-roll methods under ambient conditions. *Sol. Energy Mater. Sol. Cells* **2011**, *95*, 1293–1302. [CrossRef]
6. Henry, C.H. Limiting efficiencies of ideal single and multiple energy gap terrestrial solar cells. *J. Appl. Phys.* **1980**, *51*, 4494–4500. [CrossRef]
7. Green, M.A.; Emery, K.; Hishikawa, Y.; Warta, W. Solar cell efficiency tables (version 35). *Prog. Photovolt. Res. Appl.* **2010**, *18*, 144–150. [CrossRef]
8. Venkatachalam, M.; Kannan, M.D.; Jayakumar, S.; Balasundaraprabhu, R.; Muthukumarasamy, N. Effect of annealing on the structural properties of electron beam deposited CIGS thin films. *Thin Solid Films* **2008**, *516*, 6848–6852. [CrossRef]
9. Čampa, A.; Krč, J.; Malmström, J.; Edoff, M.; Smole, F.; Topič, M. The potential of textured front ZnO and flat TCO/metal back contact to improve optical absorption in thin Cu(In,Ga)Se_2 solar cells. *Thin Solid Films* **2007**, *515*, 5968–5972. [CrossRef]
10. Powalla, M.; Cemernjak, M.; Eberhardt, J.; Kesslera, F.; Kniesea, R.; Mohring, H.D.; Dimmler, B. Large-area CIGS modules: Pilot line production and new developments. *Sol. Energy Mater. Sol. Cells* **2006**, *90*, 3158–3164. [CrossRef]
11. Alsema, E.; de Wild-Scholten, M.J. Environmental Impacts of Crystalline Silicon Photovoltaic Module Production. In Proceedings of the 13th CIRP International Conference on Life Cycle Engineering, Leuven, Belgium, 31 May–2 June 2006.
12. Kaelin, M.; Rudmann, D.; Tiwari, A.N. Tiwari, Low cost processing of CIGS thin film solar cells. *Sol. Energy* **2004**, *77*, 749–756. [CrossRef]
13. Panthani, M.G.; Akhavan, V.; Goodfellow, B.; Schmidtke, J.P.; Dunn, L.; Dodabalapur, A.; Korgel, B.A. Synthesis of $CuInS_2$, $CuInSe_2$, and Cu(InxGa1-x)Se_2 (CIGS) nanocrystal "inks" for printable photovoltaics. *J. Am. Chem. Soc.* **2008**, *130*, 16770–16777, [b] Ram Kumar, J., Ananthakumar, S. & Moorthy Babu, S. Journal of Elec Materi (2017) 46: 296. [CrossRef] [PubMed]

14. Guillemoles, J.F.; Kronik, L.; Cahen, D.; Rau, U.; Jasenek, A.; Schock, H.W. Stability issues of Cu(In,Ga)Se_2 -based solar cells. *J. Phys. Chem. B* **2000**, *104*, 4849–4862. [CrossRef]
15. Stappert, S.; Rellinghaus, B.; Acet, M.; Wassermann, E.F. Gas-phase preparation of L10 ordered FePt nanoparticles. *J. Cryst. Growth* **2003**, *252*, 440–450. [CrossRef]
16. Repins, I.; Contreras, M.A.; Egaas, B.; DeHart, C.; Scharf, J.; Perkins, C.L.; Noufi, R. 19.9%-efficient ZnO/CdS/$CuInGaSe_2$ Solar Cell with 81.2% Fill Factor. *Prog. Photovolt. Res. Appl.* **2008**, *16*, 235–239. [CrossRef]
17. Choi, I.H.; Peter, Y.Y. Preparation of $CuInSe_2$/$CuGaSe_2$ two layers absorber film by meta-organic chemical vapor deposition. *Curr. Appl. Phys.* **2009**, *9*, 151–154. [CrossRef]
18. Bhattacharya, R.N. Electrodeposited two-layer Cu-In-Ga-Se/In-Se thin films. *J. Electrochem. Soc.* **2010**, *157*, D406–D410. [CrossRef]
19. Lim, Y.S.; Jeong, J.; Kim, J.Y.; Ko, M.J.; Kim, H.; Kim, B.; Lee, D.K. Binder-free Cu-In alloy nanoparticles precursor and their phase transformation to chalcogenides for solar cell applications. *J. Phys. Chem. C* **2013**, *117*, 11930–11940. [CrossRef]
20. Liu, S.H.; Chen, F.S.; Lu, C.H. Synthesis of $CuInSe_2$ films via selenizing the Cu-In alloy-containing nanopowders. *J. Alloys Compd.* **2012**, *517*, 14–19. [CrossRef]
21. Takahashi, H.; Konishi, N.; Ohno, H.; Takahashi, K.; Koike, Y.; Asakura, K.; Muramatsu, A. Preparation of well-crystallized $Pd_{20}Te_7$ alloy nanoparticulate catalysts withuniform structure and composition in liquid-phase. *Appl. Catal. A Gen.* **2011**, *392*, 80–85. [CrossRef]
22. Takahashi, H.; Mabuchi, T.; Yokoyama, S.; Tohji, K. Synthesis method for well crystallized alloy nanoparticles in aqueous solution under room temperature by controlling the metal complexes condition. In *Nanotechnology 2013: Advanced Materials, CNTs, Particles, Films and Composites (Volume 1)*; CRC Press: Boca Raton, FL, USA, 2013.
23. Hayes, J.R.; Hodge, A.M.; Biener, J.; Hamza, A.V.; Sieradzki, K. Monolithic nanoporous copper by dealloying Mn-Cu. *J. Mater. Res.* **2006**, *21*, 2611–2616. [CrossRef]
24. Chou, N.H.; Ke, X.; Schiffer, P.; Schaak, R.E. Room-temperature chemical synthesis of shape-controlled indium nanoparticles. *J. Am. Chem. Soc.* **2008**, *130*, 8140–8141. [CrossRef] [PubMed]
25. Badawy, W.A.; El-Rabiee, M.M.; Helal, N.H.; Nady, H. Effect of nickel content on the electrochemical behavior of Cu-Al-Ni alloys in chloride free neutral solutions. *Electrochim. Acta* **2010**, *56*, 913–918. [CrossRef]
26. Caballero-Briones, F.; Palacios-Padrós, A.; Sanz, F. CuInSe2 films prepared by three step pulsed electrodeposition. Deposition mechanisms, optical and photoelectrochemical studies. *Electrochim. Acta* **2011**, *56*, 9556–9567. [CrossRef]
27. Tsujiguchi, M. Indium Recovery and Recycling from an LCD Panel. In *Design for Innovative Value Towards a Sustainable Society*; Springer Science + Business Media: Berlin, Germany, 2012; pp. 743–746.
28. Massalski, T.B.; Okamoto, H. *Binary Alloy Phase Diagrams*, 2nd ed.; ASM International: Minerals Park, OH, USA, 1990; pp. 1424–1426.
29. Okamoto, H. Cu−In (Copper−Indium). *J. Phase Equilib. Diffus.* **2005**, *26*, 645. [CrossRef]
30. Simic, V.; Marinkovic, Z. Room temperature interactions in copper-metal thin film couples. *J. Less Common Met.* **1980**, *72*, 133–140. [CrossRef]
31. Roy, R.; Pradhan, S.K.; De, M.; Sen, S.K. Structural characterization of the CuIn intermetallic phase produced by interfacial reactions in Cu/In bimetallic films. *Thin Solid Films* **1993**, *229*, 140–142. [CrossRef]
32. Orbey, N.; Birkmire, R.W.; Russell, T.F.; Jones, G.A. Copper-indium alloy transformations. *J. Phase Equilib.* **2000**, *21*, 509–513. [CrossRef]
33. Pisarkiewicz, T.; Jankowski, H.; Schabowska-Osiowska, E.; Maksymowicz, L.J. Fabrication of thin film polycrystalline CIS photovoltaic heterostructure. *Opto-Electron. Rev.* **2003**, *11*, 297–304.
34. Yan, Y.-H.; Liu, Y.-C.; Fang, L.; Zhu, J.-S.; Zhao, H.-H.; Li, D.-R.; Lu, Z.-C.; Zhou, S.-X. Characterization of $CuInS_2$ thin films prepared by sulfurization of Cu-In precursor. *Trans. Nonferrous Met. Soc. China* **2008**, *18*, 1083–1088. [CrossRef]
35. Chang, J.; Lee, J.H.; Cha, J.H.; Jung, D.Y.; Choi, G.; Kim, G. Bimetallic nanoparticles of copper and indium by borohydride reduction. *Thin Solid Films* **2011**, *519*, 2176–2180. [CrossRef]
36. Shin, H.S.; Yang, H.J.; Kim, S.B.; Lee, M.S. Mechanism of growth of colloidal silver nanoparticles stabilized by polyvinyl pyrrolidone in γ-irradiated silver nitrate solution. *J Colloid Interface Sci.* **2004**, *274*, 89–94. [CrossRef] [PubMed]

37. Agnihotri, O.P.; Ram, P.R.; Thangaraj, R.; Sharma, A.K.; Raturi, A. Structural and optical properties of sprayed $CuInSe_2$ films. *Thin Solid Films* **1983**, *102*, 291–297. [CrossRef]
38. Schmid, D.; Ruckh, M.; Grunwald, F.; Schock, H.W. Chalcopyrite/defect chalcopyrite heterojunctions on the basis of $CulnSe_2$. *J. Appl. Phys.* **1993**, *73*, 2902–2909. [CrossRef]
39. Park, J.H.; Yang, I.S.; Cho, H.Y. Micro-raman spectroscopy on polycrystalline $CulnSe_2$ formation. *Appl. Phys. A* **1994**, *58*, 125–128. [CrossRef]
40. Bodnar, I.V.; Gremenok, V.F.; Schmitz, W.; Bente, K.; Doering, T. Preparation and investigation of (CuInSe2)x(2ZnSe)1-x and (CuInTe2)x(2ZnTe)1-x solid solution crystals. *Cryst. Res. Technol.* **2004**, *39*, 301–307. [CrossRef]
41. Brummer, A.; Honkimäki, V.; Berwian, P.; Probst, V.; Palm, J.; Hock, R. Formation of $CuInSe_2$ by the annealing of stacked elemental layers—Analysis by in situ high-energy powder diffraction. *Thin Solid Films* **2003**, *437*, 297–307. [CrossRef]
42. Izquierdo-Roca, V.; Saucedo, E.; Ruiz, C.M.; Fontané, X.; Calvo-Barrio, L.; Álvarez-Garcia, J.; Bermudez, V. Raman scattering and structural analysis of electrodeposited $CuInSe_2$ and S-rich quaternary $CuIn(S.,Se)_2$ semiconductors for solar cells. *Phys. Status Solidi A* **2009**, *206*, 1001–1004. [CrossRef]
43. Hibberd, C.J.; Ernits, K.; Kaelin, M.; Müller, U.; Tiwari, A.N. Chemical incorporation of copper into indium selenide thin-films for processing of $CuInSe_2$ solar cells. *Prog. Photovolt. Res. Appl.* **2008**, *16*, 585–593. [CrossRef]
44. Rincón, C.; Ramirez, F.J. Lattice vibrations of $CuInSe_2$ and $CuGaSe_2$ by raman microspectrometry. *J. Appl. Phys.* **1992**, *72*, 4321–4324. [CrossRef]
45. Minceva-Sukarova, B.; Najdoski, M.; Grozdanov, I.; Chunnilall, C.J. Raman spectra of thin solid films of some metal sulfides. *J. Mol. Struct.* **1997**, *410*, 267–270. [CrossRef]
46. Chang, C.H.; Davydov, A.; Stanbery, B.J.; Anderson, T.J. The conference record of the 25th IEEE photovoltaic specialists conference. In Proceedings of the 25th IEEE Photovoltaic Specialists Conference, Washington, DC, USA, 13–17 May 1996; p. 849.
47. Hegedus, S.S.; Shafarman, W.N. Thin-film solar cells: Device measurements and analysis. *Prog. Photovolt.* **2004**, *12*, 155–176. [CrossRef]
48. Lundberg, O.; Bodegård, M.; Malmström, J.; Stolt, L. Influence of the $Cu(In,Ga)Se_2$ thickness and Ga grading on solar cell performance. *Prog. Photovolt. Res. Appl.* **2003**, *11*, 77–88. [CrossRef]



© 2018 by the authors. Licensee MDPI, Basel, Switzerland. This article is an open access article distributed under the terms and conditions of the Creative Commons Attribution (CC BY) license (http://creativecommons.org/licenses/by/4.0/).